Journal of
Marine Science and Engineering

MDPI

Article

Theoretical and Numerical Study of Eddy Current Pulsed Thermography to Detect Damage of Deep-Sea Manned Pressure Hull

Yu Wu [1], Chaohua Zhang [1], Fang Wang [1] and Chao Yang [2,*]

[1] Shanghai Engineering Research Center of Hadal Science and Technology, College of Engineering Science and Technology, Shanghai Ocean University, Shanghai 201306, China; wuyu314159262@163.com (Y.W.); wangfang@shou.edu.cn (F.W.)
[2] Merchant Marine College, Shanghai Maritime University, Shanghai 201306, China
* Correspondence: yc9316@163.com

Abstract: At present, research on pressure hull safety is mainly focused on the constitutive model of material properties and the evaluation model of structural parameters aiming at fatigue life prediction. The damage identification and quantitative evaluation methods of pressure hulls have not been studied. In this study, an eddy current thermal imaging method is introduced to detect micro-cracks in a deep-sea spherical pressure hull. In the detection method, temperature is used as a parameter to identify and quantify cracks. The temperature distribution around the cracks is studied using theoretical analysis and finite element simulation. A theoretical model is established using electromagnetic theory and heat transfer theory. Moreover, the temperature difference between the cracked area and the non-cracked area can be obtained by solving the heat conduction equation. A pulsed eddy current thermal imaging testing system is established, and a defective titanium alloy specimen is tested. At the same time, the temperature around the cracks in the specimens is simulated. The specimens have the same material and welding as a deep-sea spherical pressure hull. This paper discusses the possibility of its use in a pressure hull, which will provide a reference for micro-crack damage identification and quantitative evaluation of a deep-sea spherical pressure hull.

Keywords: deep-sea; manned submersible; micro crack; eddy current

check for updates

Citation: Wu, Y.; Zhang, C.; Wang, F.; Yang, C. Theoretical and Numerical Study of Eddy Current Pulsed Thermography to Detect Damage of Deep-Sea Manned Pressure Hull. *J. Mar. Sci. Eng.* **2023**, *11*, 1410. https://doi.org/10.3390/jmse11071410

Academic Editors: Kazem Reza Kashyzadeh and Mahmoud Chizari

Received: 25 June 2023
Revised: 8 July 2023
Accepted: 9 July 2023
Published: 14 July 2023

1. Introduction

The pressure hull is a critical component of deep-sea manned submersibles and provides a safe environment for pilots and scientists [1]. Deep-sea pressure hulls are mostly made of high-strength materials and built with large and thick welded components. For example, the pressure hull of the "Jiaolong" manned submersible is welded with multiple pieces of metal, as shown in Figure 1. With the improvement in manufacturing technology, the production of spherical pressure hulls has achieved hemispheric welding in several submersibles, such as the "Deep Sea Warrior" manned submersible and the "Striver" manned submersible. However, the welded parts at the access hatch and observation windows are weak and threaten the safety of the pressure hull. Extreme working environments will cause stress concentrations and micro-cracks in the strengthened positions of the pressure hull. Therefore, the damage identification and quantitative evaluation of deep-sea spherical pressure hulls are crucial.

The following aspects of health-monitoring methods of marine structures were studied. (1) Health monitoring is based on the principle of strain detection. Lindemann et al. [2] implemented a hull structure monitoring system based on the principle of strain detection. Yang Huawei et al. [3] analyzed the force of a submersible pressure hull, determined the sensor arrangement, designed a structural health monitoring and evaluation system for a spherical pressure hull, and studied the creep effect on the monitoring system. (2) Health

monitoring is based on the principle of acoustic signals. Angulo et al. [4] monitored the initiation and propagation of fatigue cracks in mooring chains using the acoustic method and designed a 72-day large-scale experiment to detect the damage to the mooring chains. Guan et al. [5] monitored the health of submarine pipelines via acoustic waves, formed a mobile mapping system using onboard sensors and underwater probes to extract a route, and buried depth information from acoustic images to monitor the status of the pipelines. Hu et al. [6] derived the Lamb wave equation according to the relevant theory and used the reflection and transmission of the Lamb wave at the crack to study the location and imaging of the crack damage in the welded steel plate. (3) Health monitoring is based on the principle of optical signals. Matine and Drissi-Habti [7] used fiber-optic sensors to analyze the damage to marine conductors used in floating marine renewable energy equipment. Mieloszyk and Ostachowicz [8] monitored the damage to offshore wind turbine support structures (tripods) based on grating sensors. (4) When the machine breaks down, there is an abnormal sound, temperature, or vibration; the vibration can directly reflect the operating conditions of the mechanical equipment. Health monitoring is based on the principle of vibration signals. The vibration signals are analyzed and processed to obtain the health of marine structures. The running state of the machine can be obtained via vibration monitoring. Targeted maintenance is carried out at an early stage of equipment failure [9–12].

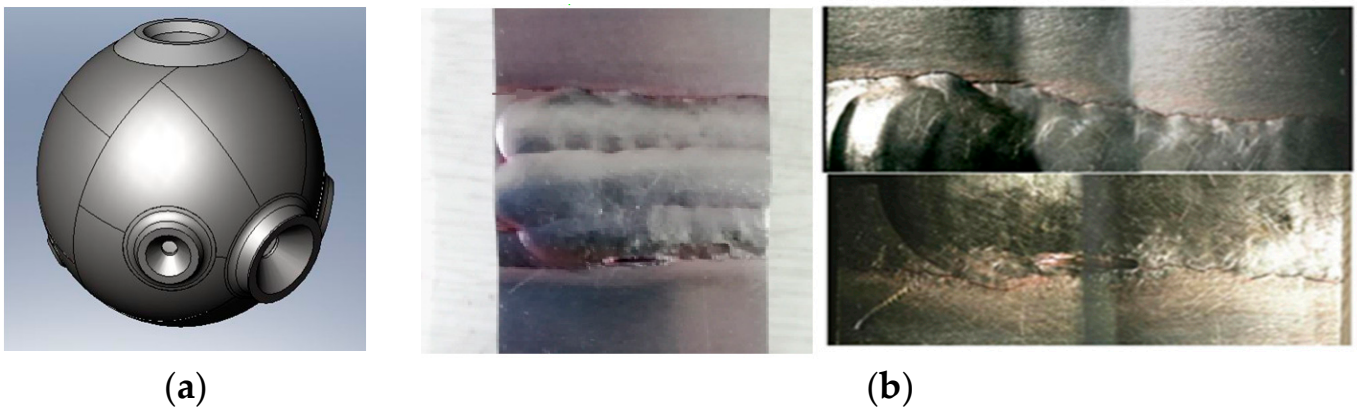

Figure 1. Schematic of the pressure hull and welding seam. (**a**) Schematic of "Jiaolong" pressure hull; (**b**) welding seam.

However, the damage identification and quantitative evaluation methods of pressure hulls have not been studied. Pulsed eddy current thermal imaging detection technology is an active infrared thermal imaging method that uses high-frequency alternating current to generate eddy currents on the surface of the specimen. According to Joule's law, part of the eddy current is converted into Joule heat—which propagates on the surface and inside the specimen—and the temperature of the specimen surface changes. When defects exist in the specimen, the eddy current is circumferential, and the Joule heat distribution is abnormal. The temperature anomaly can be detected using an infrared thermal imager.

This technology has the advantages of causing no pollution and having no contact, high resolution of the thermal imager, high detection efficiency, and visual imaging results. However, because eddy current pulsed thermal imaging couples the eddy current field with the thermal field, surface defects can directly affect the distribution of the eddy current field, and at the same time, the thermal field distribution of the defect area is disturbed. More features could be extracted for crack detection, and the detection effect would be better. Moreover, eddy current heating can directly heat the inside of the workpiece within the range of skin depth. On this basis, the thermal diffusion transmission depth is larger, and deeper crack defects can be detected via thermal diffusion. Therefore, the influence of the skin effect on depth detection in eddy current testing can be overcome.

However, quantifying micro-cracks accurately is difficult. Defect detection and quantitative recognition are affected by many aspects, such as the electrical properties, thermal properties, surface properties of the specimen, and the lift-off height of the coil (the distance between the coil and the specimen surface). So, it is difficult to accurately confirm the crack size. At present, defect detection within the skin depth of conductive materials is relatively accurate, whereas defect detection beyond the skin depth and in non-conductive materials is difficult.

Xu et al. [13] recently proposed scanning eddy current thermography under AC-DC composite magnetization to fulfill scanning detection and quantify the defect in bearing rings. Dirahoui et al. [14] presented numerical and experimental investigations of the structural control of multilayer high-temperature superconducting (HTS) tapes. Ding et al. [15] proposed a statistical approach for paint-coated S275 steel corrosion evaluation based on ECPT. Lee et al. [16] performed defect detection on the subsurface of the STS304 metal specimen by applying the line-scanning method to induction thermography. Liang et al. [17] used eddy current pulsed thermography (ECPT) to detect rolling contact fatigue (RCF) cracks in the rail. Tu et al. [18] proposed a method based on ECPT combined with feature extraction transform algorithms for transient thermal pattern separation and defect detection in composite insulators with internal conductive defects. Liu et al. [19] used ECPT in the characterization of RCF cracks in the rail by taking advantage of electromagnetic thermal execution. Hernandez et al. [20] performed pulsed phase thermography using electromagnetic coil excitation to capture thermal transient localized responses for defect characterization. Zou et al. [21] proposed ECPT for the nondestructive evaluation of carbon-fiber-reinforced polymer (CFRP) steel interface. Four CFRP steel specimens with different shapes and sizes of interface defects were tested. Chen et al. [22] presented a scanning induction thermography (SIT) system for the automatic detection of drill pipe thread (DPT).

In addition, Ren et al. [23] used thermal variations to quantify the current amplitude and reconstruct the current direction based on the passivity of the electric field. Xie et al. [24] developed a local region-based strategy to identify these crack regions from the ECPT inspection data using a supervised classification procedure. Zhang et al. [25] investigated thermography data compression using several unsupervised learning (UL) algorithms to compress different data types. Barakat et al. [26] used a low-power eddy current imaging experimental device to detect, locate, and determine surface cracks in strip samples. And the size of the cracks can be obtained from the temperature gradient of the image. Yi et al. [27] found that the eddy current thermal imaging technology has significant lateral thermal diffusion, which causes a large error in the quantitative evaluation of crack depth. Oswald-Tranta et al. [28] reported that there must be a short heating pulse in non-ferromagnetic material with high electrical and thermal conductivity; otherwise, the thermal signal will decrease quickly. Souridi et al. [29] obtained reliable crack detection results using simple digital image processing methods to replace computationally intensive and time-consuming data processing techniques, and the cracks were detected and identified.

In this paper, the eddy current thermal imaging method is introduced to detect micro-cracks in a deep-sea spherical pressure hull, which has the advantages of non-contact, intuitive detection results, and so on. As a parameter to identify and quantify cracks, the temperature distributions of the cracks are studied using theoretical analysis, experimental tests, and finite element simulations. The paper also discussed the possibility of its use in pressure hulls to provide a reference for the micro-crack damage identification and quantitative evaluation of deep-sea spherical pressure hulls. The theoretical analysis process and finite element analysis process are shown in Figure 2.

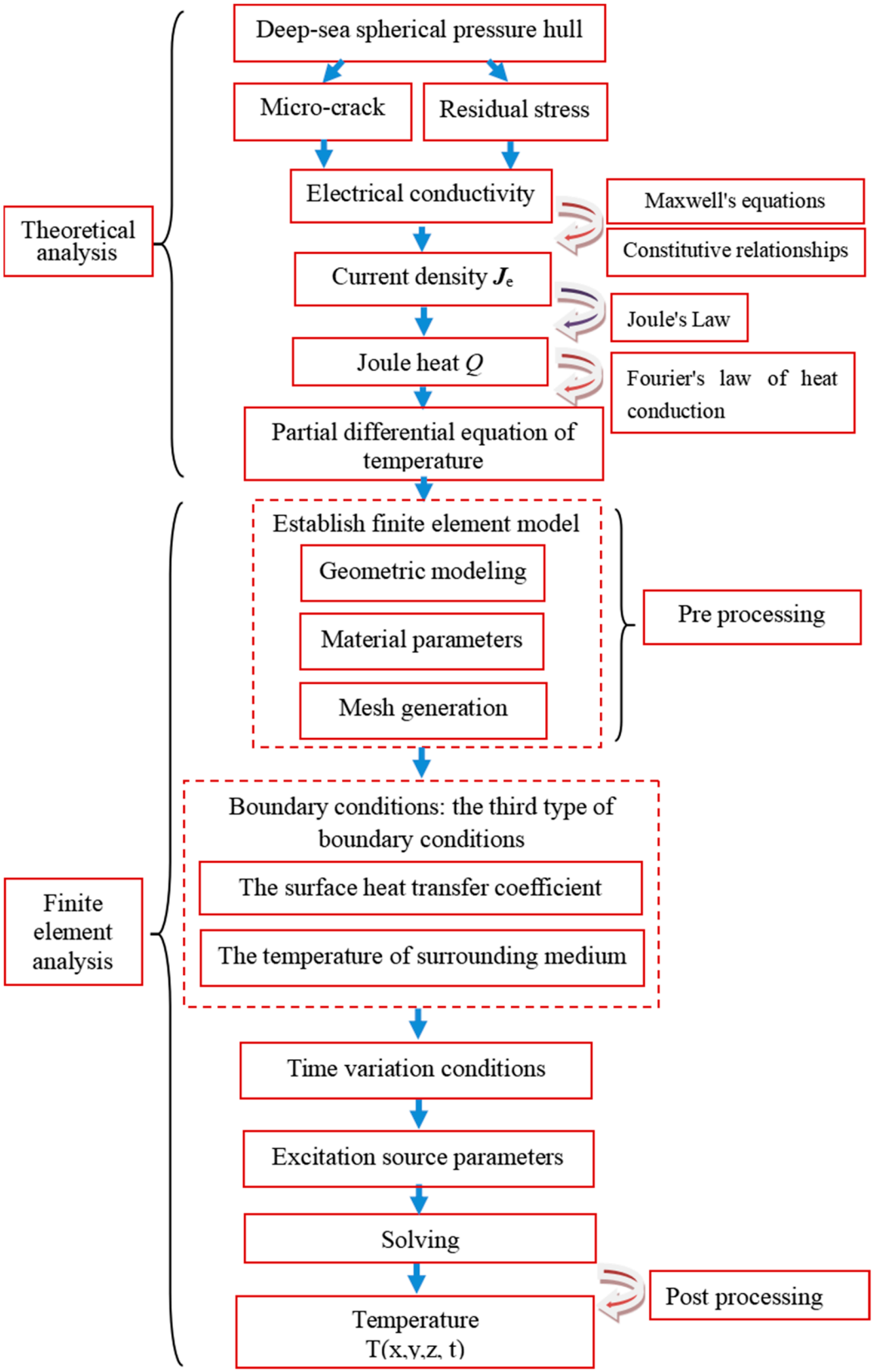

Figure 2. The theoretical analysis and finite element analysis process.

2. Theoretical Analysis

When an alternating current passes through the excitation coil, an induced magnetic field is generated due to the effect of electromagnetic induction. The intensity of the magnetic induction is related to the magnitude of the excitation current, which can be expressed as

$$\nabla \times \boldsymbol{H} = \boldsymbol{J} + \frac{\partial \boldsymbol{D}}{\partial t} \tag{1}$$

$$\nabla \times \boldsymbol{E} = -\frac{\partial \boldsymbol{B}}{\partial t} \tag{2}$$

$$\nabla \cdot \boldsymbol{B} = 0 \tag{3}$$

$$\nabla \cdot \boldsymbol{D} = \rho \tag{4}$$

where $\boldsymbol{J}$ is the current density, $\boldsymbol{D}$ is the electric displacement vector, $\boldsymbol{H}$ is the magnetic field intensity, $\boldsymbol{E}$ is the electric field intensity, $\boldsymbol{B}$ is the magnetic induction intensity, ρ is the charge density, and t is the time.

In addition to Equations (1)–(4), the constitutive relationships are as follows: $\boldsymbol{J} = \sigma \boldsymbol{E}$, $\boldsymbol{D} = \varepsilon \boldsymbol{E}$, and $\boldsymbol{B} = \mu \boldsymbol{H}$, where ε is the permittivity, μ is the permeability, and σ is the electrical conductivity. In addition, a vector magnetic potential $\boldsymbol{A}$ that satisfies the Coulomb specification is introduced as follows:

$$\nabla \cdot (\nabla \times \boldsymbol{A}) = 0 \tag{5}$$

Using Equations (3) and (5), the following equations can be obtained:

$$\boldsymbol{B} = \nabla \times \boldsymbol{A} \tag{6}$$

$$\boldsymbol{E} = -\frac{\partial \boldsymbol{A}}{\partial t} - \nabla V \tag{7}$$

where V is the scalar potential.

Equations (6)–(7) are substituted into the current law Equation (1), and the time-varying equation of the eddy current excitation can be obtained as follows:

$$\nabla \times \left(\frac{1}{\mu} \nabla \times \boldsymbol{A} \right) + \boldsymbol{J}_e = \boldsymbol{J}_s \tag{8}$$

$$\boldsymbol{J}_e = \sigma \frac{\partial \boldsymbol{A}}{\partial t} \tag{9}$$

where $\boldsymbol{J}_s$ represents the current density passing through the coil and $\boldsymbol{J}_e$ represents the current density generated by electromagnetic induction. The finite element method is used to solve the above equations, and the eddy current distribution inside the metal can be obtained using the following equation:

$$\boldsymbol{J}_e(z) = \boldsymbol{J}_e(0) \cdot e^{-z\sqrt{\pi \mu \sigma f}} \tag{10}$$

where z represents the depth of the specimen. It is observed that eddy current density decreases with increasing depth. When an alternating current passes through the coil, an eddy current at the same frequency as the excitation coil is generated inside the pressure hull due to electromagnetic induction.

It is also observed that the density of the eddy current decays rapidly from the surface to the interior of the pressure hull. When the eddy current decays from the surface of the metal to $1/e$ of the surface, the penetration depth at this time is called the skin depth, which can be calculated as follows: $\delta = 1/\sqrt{\pi\mu\sigma f}$, where f represents the frequency of the excitation current. When the current I passes through the excitation coil, the magnetic induction intensity $\boldsymbol{B}$ around the excitation coil satisfies the following equation: $\boldsymbol{B} = \mu I/2\pi h$, where h represents the distance from the excitation coil. As the distance h increases, the magnetic induction around the excitation coil gradually decreases. The metal is a closed loop, and the eddy current is converted into Joule heat inside the metal. The thermal power P_w is proportional to the electric field strength $\boldsymbol{E}$ and the eddy current density $\boldsymbol{J}_e$: $P_w = \frac{1}{\sigma}|\sigma\boldsymbol{E}|^2 = \frac{1}{\sigma}|\boldsymbol{J}_e|^2$.

The Joule heat Q spreads inside the pressure hull as follows:

$$\rho C_p \frac{\partial T(z,t)}{\partial t} - \nabla(k\nabla T(z,t)) = Q \tag{11}$$

where z is the distance from the surface of the pressure hull; $T(z, t)$ is the temperature at (location z, time t); Q is the heat source; k is the thermal conductivity; C_p is the specific heat capacity of the metal. By solving the heat conduction equation, the temperature $T(z, t)$ can be expressed as

$$T(z,t) = \frac{Q}{\sqrt{\pi\rho C_p k t}} \exp\left(-\frac{z^2}{4\alpha t}\right) \tag{12}$$

where α is the thermal diffusivity, which can be expressed as $\alpha = k/\rho C_p$.

During the test, only the surface temperature of the pressure hull can be obtained. The temperature on the surface of the pressure hull with no crack ($z = 0$) can be expressed as

$$T_n(0,t) = \frac{Q}{\sqrt{\pi\rho C_p k t}} \tag{13}$$

If there is a crack inside the test piece, the distance between the crack and the surface is d, and the heat wave is reflected and propagated, then the surface temperature of the test piece in the crack area can be expressed as

$$T_d(0,t) = \frac{Q}{\sqrt{\pi\rho C_p k t}} \left(1 + 2\exp\left(-\frac{d^2}{\alpha t}\right)\right) \tag{14}$$

An infrared thermal imager is used to record the temperature variation on the surface of the test piece, which is used to determine the crack parameter. The temperature difference between the cracked area and the non-cracked area can be expressed as

$$\Delta T = T_d(0,t) - T_n(0,t) = \frac{2Q}{\sqrt{\pi\rho C_p k t}} \exp\left(-\frac{d^2}{\alpha t}\right) \tag{15}$$

By differentiating the above equation, the time when the maximum temperature difference occurs can be expressed as

$$t_{\max} = 2d^2/\alpha \tag{16}$$

The characteristic value is called the peak time, which characterizes the depth d of the crack from the surface and the thermal diffusivity α of the material. In addition, other characteristic values can be extracted to detect and evaluate cracks, or to measure material properties.

It should be noted that if the metal is a ferromagnetic material, the skin depth is smaller than the thickness of the specimen, and the skin depth is so small that it can be ignored. Therefore, the heat generation process can be simplified, as the heat is directly formed on the surface of the specimen [30]. The one-dimensional analytical heat transfer model with no damage can be expressed as

$$T(t) = \frac{Q}{\rho C_p L}\left[1 + 2\sum_{n=1}^{\infty}(-1)^n \exp\left(-\frac{n^2\pi^2}{L^2}\alpha t\right)\right] \tag{17}$$

where Q is the surface heat of the specimen, ρ is the density, C_p is the specific heat capacity, L is the thickness of the specimen, and α is the thermal diffusivity. And the one-dimensional heat transfer model with a crack can be expressed as

$$T_d(t) = \frac{Q_d}{\rho C_p L_d}\left[1 + 2\sum_{n=1}^{\infty}(-1)^n \exp\left(-\frac{n^2\pi^2}{{L_d}^2}\alpha t\right)\right] \tag{18}$$

where L_d is the depth of the crack and Q_d is the Joule heat on the crack.

3. Experimental Equipment

The pulsed eddy current thermal imaging testing system is shown in Figure 3, which consists of three parts: a computer image processing system, an infrared thermal imager, and an induction heating system (induction heater, circulating water cooler, and excitation coil). The tested specimen is heated using an induction heating system, and the surface temperature of the specimen is recorded using an infrared thermal imager. The thermal imager used in the experiment is a Fotric348L infrared thermal imager manufactured by FOTRIC in the United States. The infrared pixel size is 640 × 480, 307,200 pixels, the temperature range is −20 °C–650 °C, the temperature sensitivity is 0.03 °C, and the display screen is a 5-inch touch screen with a 1280 × 720 resolution ratio. The induction heating system is BS-05KW EASYHEAT induction heating equipment manufactured by Guangzhou Huolong, Guangdong, China, which can generate high-frequency electromagnetic signals with a frequency range of 150–400 KHz and a power of 3 KW in the excitation coil.

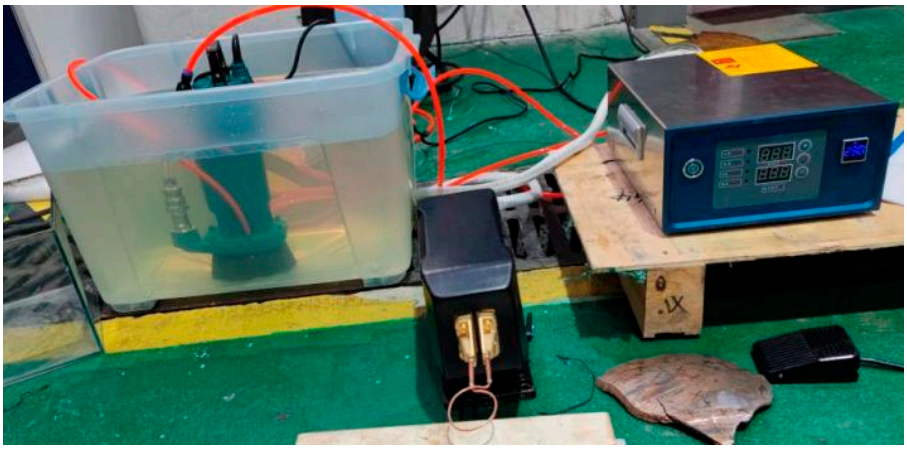

Figure 3. Pulsed eddy current thermal imaging testing system.

The titanium alloy plate-tested specimen is shown in Figure 4. The material of the specimen is the titanium alloy Ti-6Al-4V, and the thickness of the sample is 9 mm. There is a defect on the edge of the sample. According to the experimental testing, the temperature at the defect location is significantly higher than that of the other parts, which is detected by the pulsed eddy current thermal imaging detection system, with a maximum temperature of 403.8 K.

(**a**) Titanium alloy plate specimen (**b**) Temperature distribution

Figure 4. Experimental measurement results.

4. Finite Element Analysis

To provide a better reference, a model with the same size, material, and weld as the manned pressure hull of the Jiaolong submersible is used. The pressure hull dimensions are shown in Figure 5a. The inner and outer diameters are 500 mm and 518 mm, respectively. It is assumed that the equatorial center of the pressure hull is welded, and the weld is a V-shaped weld, as shown in Figure 5b. The excess height is 2 mm (C), the groove angle is 60° (α), and the groove depth is 9 mm (H). The material of the pressure hull is the high-strength titanium alloy Ti-6Al-4V, and it is assumed that the welding material is the same as that of the pressure hull.

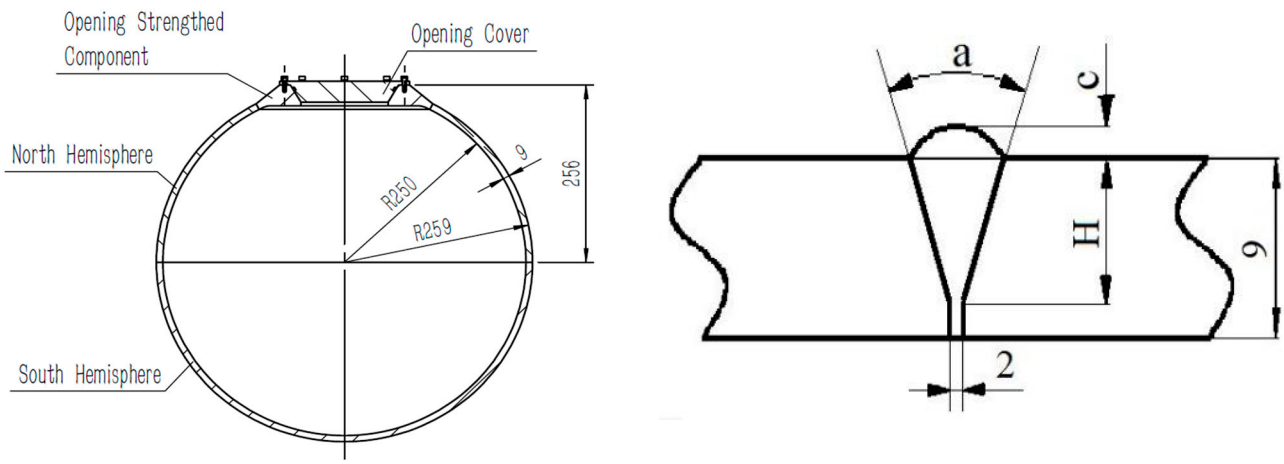

(**a**) Schematic of the spherical pressure hull (**b**) Weld structure

Figure 5. Schematic diagram of the simulated spherical pressure hull and welded structure (C is the excess height, α is the groove angle, and H is the groove depth).

The diameter of the coil is 8 mm, and the length of the coil is 100 mm. The excitation source parameters are set as follows: 255 KHz frequency, 300 A current amplitude, 1 coil turn, 300 ms heating time, 400 ms cooling time, and 700 ms calculation time. The lift-off height of the coil is 1 mm. It is assumed that the crack is a regular small rectangular shape, and the parameters of the crack are set as follows: length is 5 mm, width is 0.5 mm, and depth is 1.5 mm. The third type of boundary condition is the surface heat transfer coefficient h between the object on the boundary and the surrounding medium, and the temperature T_f of the surrounding medium is selected. In this study, the surface heat transfer coefficient h is set to 5 W/(m^2·K), and the temperature T_f is set to 293.15 K.

The dynamic distribution of the temperature near the crack on the weld surface is shown in Figure 6 (temperature unit: K). The temperature under the coil is the highest, the temperature gradually decreases along the periphery, and the eddy current is along the direction of the weld. In the heating and cooling process, the thermal diffusion rate along the length direction of the weld is greater than the thermal diffusion rate in the width direction.

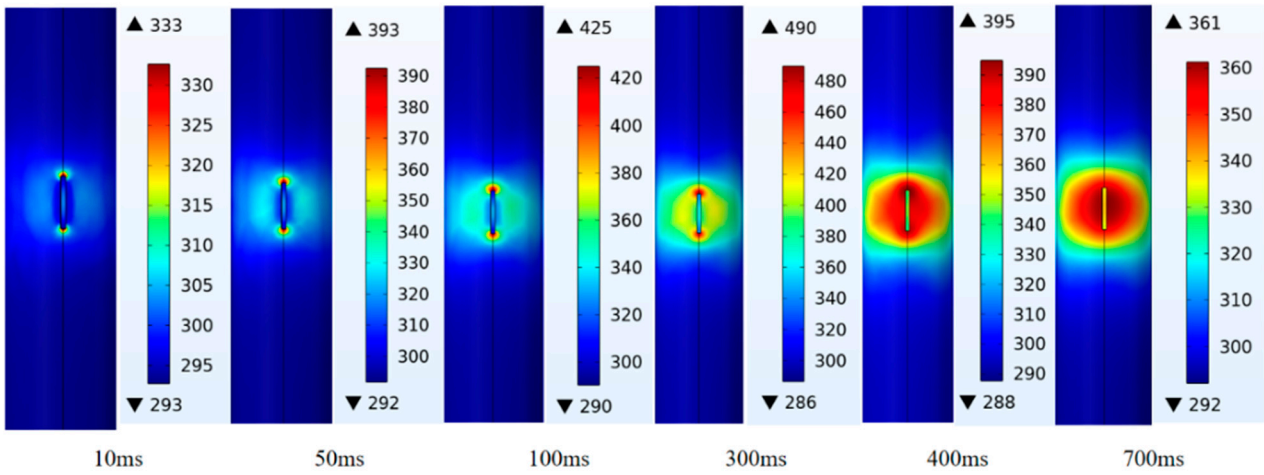

Figure 6. Dynamic temperature distribution of surface crack of the pressure hull.

Feature points are selected to analyze the cracks in the pressure hull. Four points on the surface of the weld are selected as the characteristic points: feature point 1 is at the crack end; feature points 2–4 are at the non-crack area. The dynamic temperature variations during the heating and cooling process are shown in Figure 7. It is shown that the temperature at both ends of the crack is higher than the temperature at the side of the crack, and the optimal observation time is 200~300 ms, indicating that the appropriate observation time is around the end of heating.

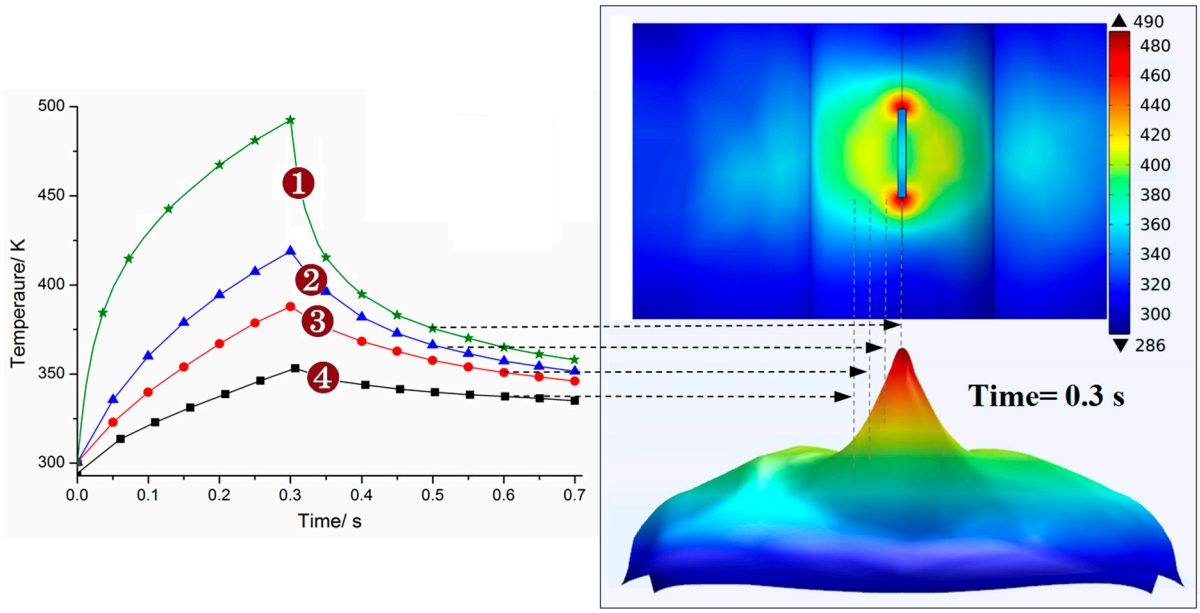

Figure 7. Surface crack temperature variations in the pressure hull with time.

In addition to surface cracks, embedded cracks are generated under the metal surface. Most of the embedded cracks are generated during the manufacturing process. The temperature distribution is 300 ms at the end of the heating. The temperature distributions of the surface crack of the pressure shell at the end of heating with and without welding are shown in Figures 8 and 9, respectively.

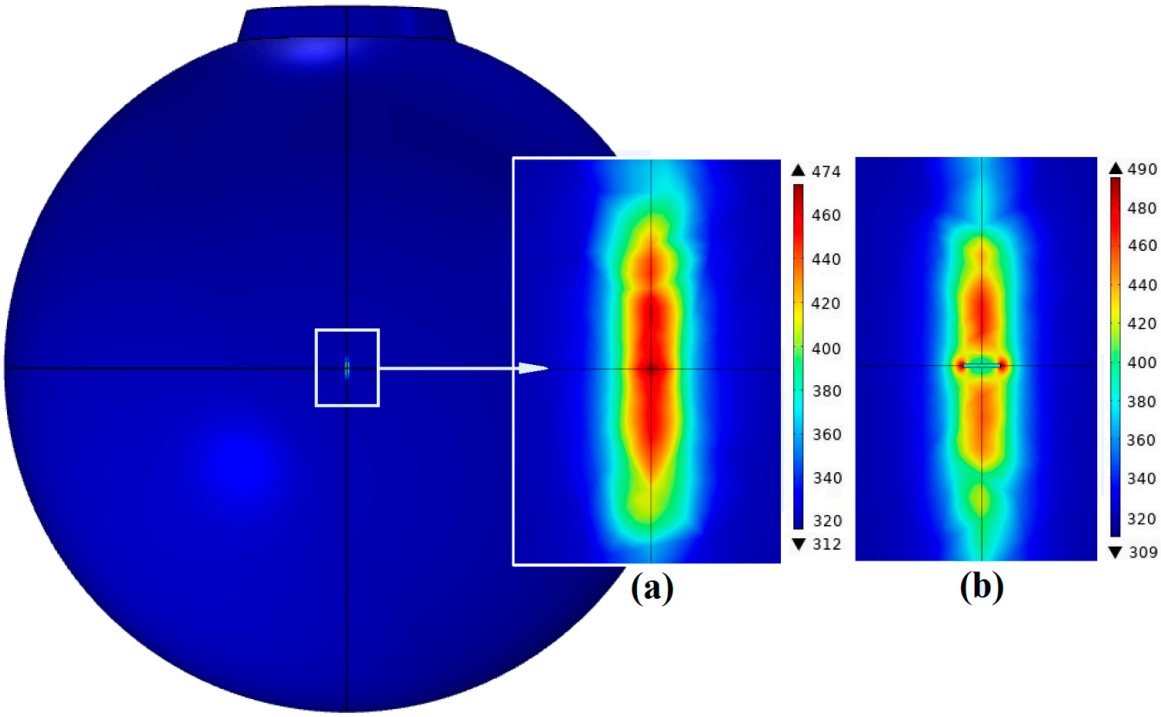

Figure 8. Temperature distribution of surface crack of pressure shell with no welding: (**a**) embedded crack; (**b**) surface crack.

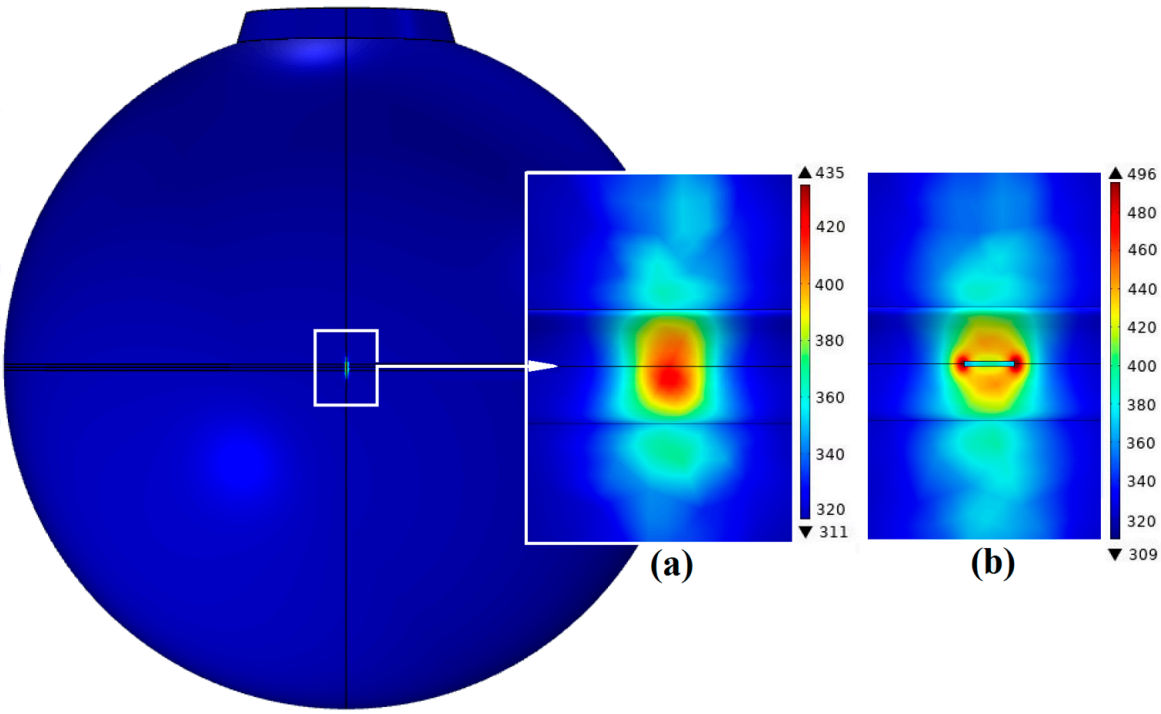

Figure 9. Temperature distribution of surface crack of pressure shell with welding: (**a**) no crack; (**b**) surface crack.

The 3D temperature distributions of the welds under different crack conditions are compared, as shown in Figure 10. The temperature caused by the surface crack is higher than that caused by the embedded crack. According to Ohm's law, the eddy current flows in the direction with the smallest impedance, the cracks are filled with air, and the impedance of air is infinite. When the crack is parallel to the direction of the weld seam, the resistivity at the crack is much larger than the metal, the eddy current flows along the direction of the minimum impedance, and the eddy current continues to flow around the crack and converges at the tip of the crack. Therefore, the eddy current density at the end of the crack increases significantly.

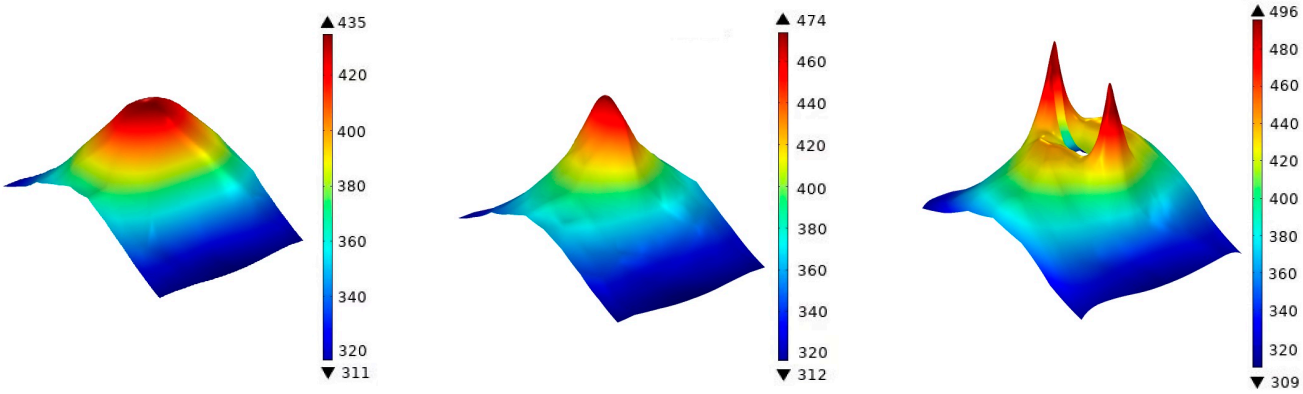

(**a**) No crack (**b**) Embedded crack (**c**) Surface crack

Figure 10. Three-dimensional temperature diagram.

During the detection process, the feature points or feature lines of abnormally high-temperature areas are selected for detection and verification, and the thermal image information is processed and extracted to detect the micro-cracks.

5. The Effect of Different Crack Parameters

5.1. The Effect of Crack Length

Different finite element models were constructed with the same crack width (w = 0.5 mm) and crack depth (d = 1.5 mm), and different crack lengths (L = 0 mm, 2.5 mm, 5 mm, and 7.5 mm). The temperature distributions for different crack lengths are shown in Figure 11.

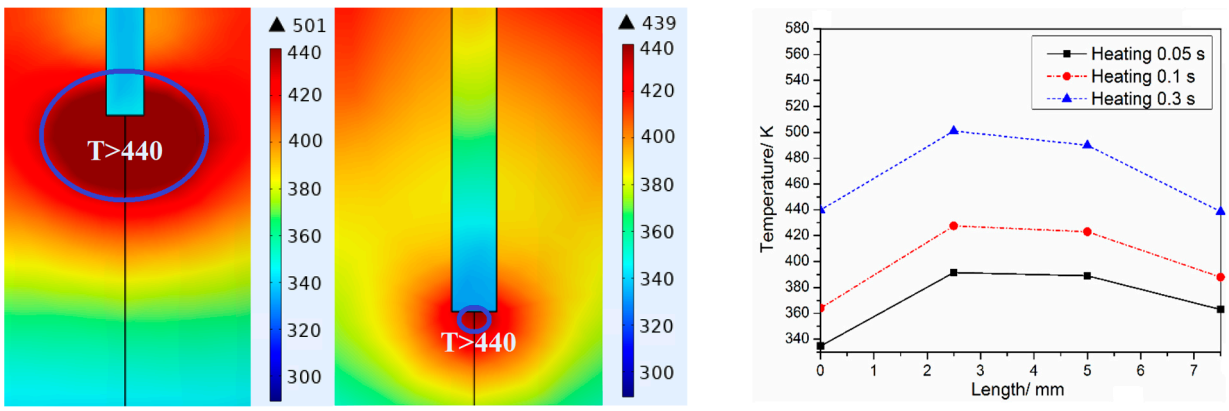

(**a**) 2.5 mm and 7.5 mm crack lengths (**b**) Different heating times

Figure 11. Temperature distributions for different crack lengths.

As shown in Figure 11, the temperature distributions at both ends of the crack are higher than those in the rest of the region; the distance between the highest temperature peaks is the length of the crack.

The high-temperature region above 440 K is smaller than the length of the crack. For example, the maximum temperature is 501 K, 490 K, and 438.6 K when the crack length is 2.5 mm, 5 mm, and 7.5 mm, respectively, at the heating time of 0.3 s, as shown in Figure 11. Because the coil is perpendicular to the crack, the temperature of the plate without cracks is the lowest. With the same crack length, the temperature increases with the heating time. The temperature variation rates caused by different crack lengths are the same at the beginning of heating. When the heating time exceeds 0.1 s, the temperature variation rate increases as the crack length increases.

5.2. The Effect of Crack Depth

Different finite element models were constructed with the same crack width (w = 0.5 mm) and crack length (L = 5 mm), and different crack depths (d = 0 mm, 1 mm, 1.5 mm, and 2 mm). The temperature distributions for different crack depths are shown in Figure 12.

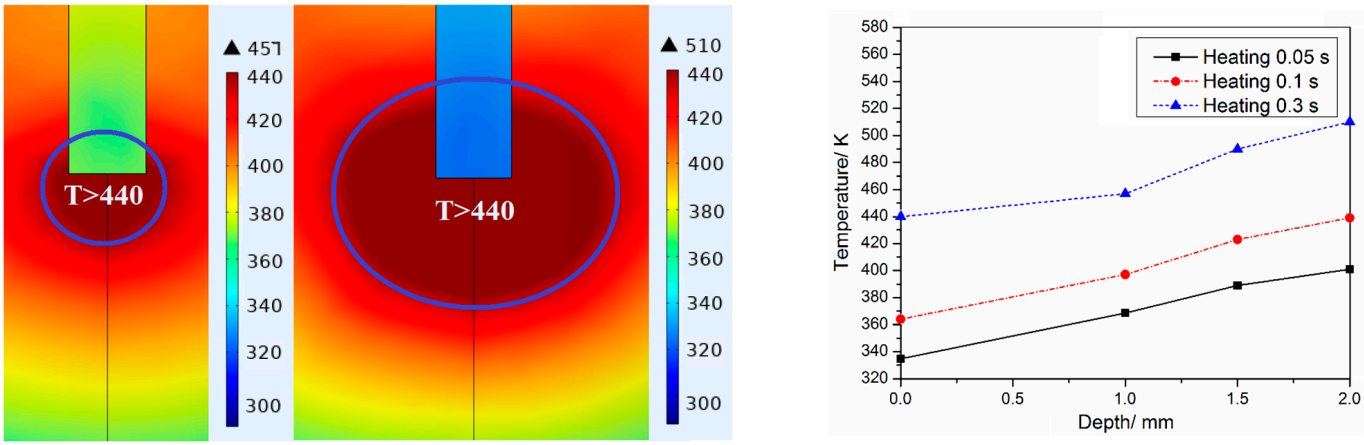

(**a**) 1 mm and 2 mm crack depths (**b**) Different heating times

Figure 12. Temperature distributions for different crack depths.

As shown in Figure 12, the high-temperature region greater than 440 K increases as the crack depth increases. For the same crack depth, the maximum temperature increases with the heating time. And the temperature at the crack tip increases as the crack depth increases; for example, the maximum temperature is 457 K, 490 K, and 510 K when the crack depth is 1 mm, 1.5 mm, and 2 mm, respectively, at the heating time of 0.3 s, as shown in Figure 12. This is because the deeper the depth, the greater the density of eddy currents gathered at the crack tip, and the higher the temperature.

5.3. The Effect of Crack Width

Finite element models were constructed with the same crack depth (d = 1.5 mm) and crack length (L = 5 mm), and different crack widths (w = 0 mm, 0.25 mm, 0.5 mm, and 1 mm). The temperature distributions for different crack widths are shown in Figure 10. The high-temperature region greater than 440 K increases as the crack width increases. For the same crack width, the maximum temperature increases with an increase in the heating time. This is because more eddy currents gather at the crack tip as the width increases, so the temperature increases with the crack width. For example, the maximum temperature is 480 K, 490 K, and 542 K when the crack width is 0.25 mm, 0.5 mm, and 1.0 mm, respectively, at the heating time of 0.3 s, as shown in Figure 13. The relationship between the crack size and maximum temperature is shown in Table 1.

Table 1. The relationship between crack size and maximum temperature.

Crack sizes/mm													
	Width	0.5	0.5	0.5	0.5	0.5	0.5	0.5	0.5	0	0.25	0.5	1
	Depth	1.5	1.5	1.5	1.5	0	1	1.5	2	1.5	1.5	1.5	1.5
	Length	0	2.5	5	7.5	5	5	5	5	5	5	5	5
Temperature/k		440	501	490	438.6	440	457	490	510	440	480	490	542

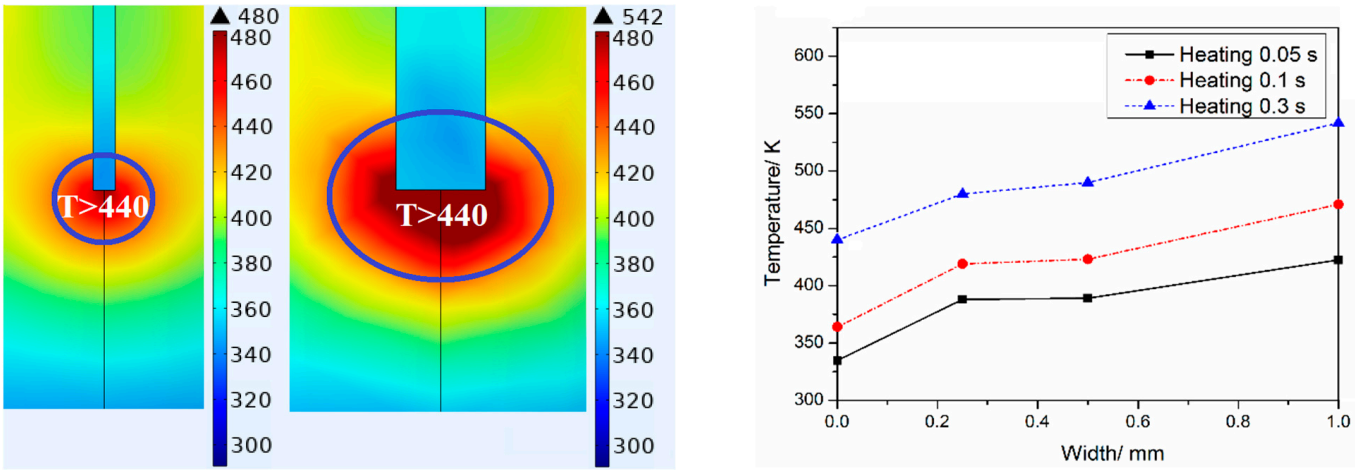

(**a**) 0.25 mm and 1 mm crack widths (**b**) Different heating times

Figure 13. Temperature distributions for different crack widths.

5.4. The Effect of Crack Angle and Coil Lift-Off Height

Cracks are caused by a variety of reasons, such as stress, restraint force, rigidity, chemical composition, weld reserved gap, weld bead, base metal cleaning, etc. [15]. The parameters of the crack are 5 mm long, 0.5 mm wide, and 1.5 mm deep. The direction of the weld crack has a certain randomness, and the direction of the crack is parallel to the weld or at a certain angle with the weld. Finite element analysis models with different crack directions are established, and the angles between the cracks and the weld are set to 0°, 30°, 45°, and 60°. The simulation results are as follows: Figure 14 shows the temperature distributions of the pressure hull surface with different crack directions after single-turn coil heating with the same excitation source. It is observed that the abnormal temperature rise is mainly concentrated at the short edges of the crack. And when the crack is not perpendicular to the coil, the "temperature noise" around the crack is large, and the crack size is difficult to obtain.

As shown in Figure 14, cracks in different directions can be detected in the titanium alloy material. And the maximum temperature decreases as the angle between the crack and the weld increases; for example, the maximum temperature is 490 K, 485 K, 480 K, and 466 K when the angle is 0°, 30°, 45°, and 60° at the heating time of 0.3 s, as shown in Figure 14b. The temperature distribution variation under different lift-off heights is shown in Figure 14. According to Ampere's theorem, the magnetic field strength of a coil is related to the current, the distance from the coil, the number of coil turns, and other factors. The eddy current and the distribution of the surface temperature are affected by the variation in lift-off height. The weld surface temperature decreases as the lift-off height increases; for example, the maximum temperature is 490 K, 433 K, 391 K, and 366 K when the lift-off height is 1 mm, 2 mm, 3 mm, and 4 mm at the heating time of 0.3 s, as shown in Figure 14c.

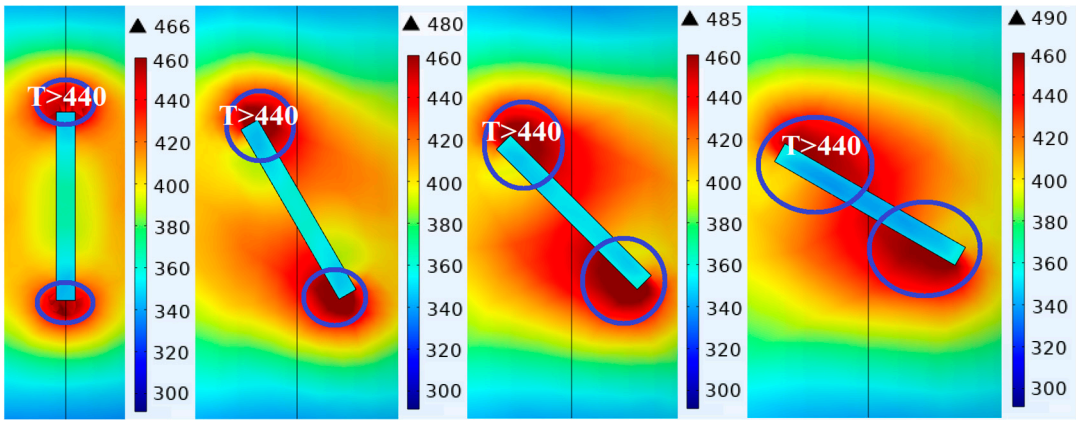

(**a**) 0°, 30°, 45°, and 60° crack angles

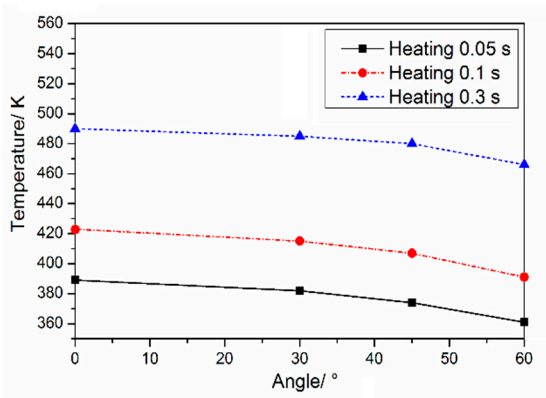

(**b**) Different crack angles

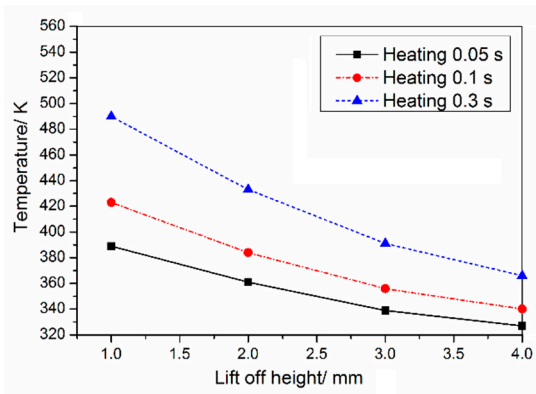

(**c**) Different lift-off heights

Figure 14. Temperature distributions for different angles and lift-off heights.

6. Conclusions

In this paper, the eddy current thermal imaging method is introduced to detect micro-cracks in deep-sea spherical pressure hulls. According to the theoretical analysis, when an alternating current passes through the coil, an eddy current at the same frequency as the excitation coil is generated inside the pressure hull due to electromagnetic induction. And the thermal power is proportional to the electric field strength and eddy current density. According to Fourier's law of heat conduction, the obtained temperature is a function of location, time, excitation source parameters, thermal conductivity, and specific heat capacity of the metal. According to the experimental testing, the temperature at the defect location is significantly higher than that of the other parts, with a maximum temperature of 403.8 K for a 9 mm titanium alloy sample. According to the finite element analysis, the temperature under the coil is the highest, the temperature gradually decreases along the periphery, and the eddy current is along the direction of the weld. In the heating and cooling process, the thermal diffusion rate along the length direction of the weld is greater than the thermal diffusion rate in the width direction. And the appropriate observation time is around the end of the heating. The temperature distributions at both ends of the crack are higher than those of the rest of the region; the distance between the highest temperature peaks is the length of the crack. The deeper the depth, the greater the density of eddy currents gathered at the crack tip, and the higher the temperature. More eddy currents gather at the crack tip as the width increases, so the temperature increases with the crack width. And, when the crack is not perpendicular to the coil, the "temperature noise" around the crack is large, and the crack size is difficult to obtain. The maximum temperature decreases as the angle between the crack and the weld increases.

Author Contributions: Conceptualization, Y.W.; methodology, C.Z.; software, C.Z.; validation, F.W.; formal analysis, C.Y.; investigation, C.Y.; resources, F.W.; data curation, Y.W.; writing—original draft preparation, F.W., and C.Y.; writing—review and editing, F.W.; supervision, Y.W.; project administration, Y.W.; funding acquisition, Y.W. All authors have read and agreed to the published version of the manuscript.

Funding: This work is supported by the National Natural Science Foundation of China (grant numbers 52101320 and 52071203).

Institutional Review Board Statement: Not applicable.

Informed Consent Statement: Not applicable.

Data Availability Statement: Not applicable.

Acknowledgments: The authors would like to express their gratitude for the support of the Fishery Engineering and Equipment Innovation Team of Shanghai High-level Local University.

Conflicts of Interest: The authors declare no conflict of interest.

References

1. Cui, W.C.; Wu, X. A Chinese strategy to construct a comprehensive investigation system for hadal trenches. *Deep Sea Res. Part II Top. Stud. Oceanogr.* **2018**, *155*, 27–33. [CrossRef]
2. Christopher, J.S.; Christopher, J.E.; Phaedon-Stelios, K. Model-based structural health monitoring of naval ship hulls. *Comput. Methods Appl. Mech. Eng.* **2011**, *200*, 1137–1149.
3. Yang, H.W.; Wan, Z.Q.; Huang, J.H.; Xiang, Y.J. Real-Time Safety Estimation Method and Experimental Validation for Deep Sea Pressure Structural Health Monitoring. *J. Ship Mech.* **2017**, *21*, 1136–1143.
4. Angulo, A.; Tang, J.L.; Khadimallah, A.; Soua, S.; Mares, C.; Gan, T.H. Acoustic Emission Monitoring of Fatigue Crack Growth in Mooring Chains. *Appl. Sci.* **2019**, *9*, 2187. [CrossRef]
5. Guan, M.L.; Cheng, Y.X.; Li, Q.Q.; Wang, C.S.; Fang, X.; Yu, J.W. An Effective Method for Submarine Buried Pipeline Detection via Multi-Sensor Data Fusion. *IEEE Access* **2019**, *7*, 125300–125309. [CrossRef]
6. Hu, M.P.; Sun, X.D.; He, J.; Zhan, Y.Y. Double Crack Damage Identification of Welded Steel Structure Based on LAMB WAVES of S0 Mode. *Materials* **2019**, *12*, 1800. [CrossRef] [PubMed]
7. Matine, A.; Drissi-Habti, M. On-Coupling Mechanical, Electrical and Thermal Behavior of Submarine Power Phases. *Energies* **2019**, *12*, 1009. [CrossRef]
8. Mieloszyk, M.; Ostachowicz, W. An application of Structural Health Monitoring system based on FBG sensors to offshore wind turbine support structure model. *Mar. Struct.* **2017**, *51*, 65–86. [CrossRef]
9. Wang, S.Q.; Xu, M.Q.; Xia, Z.P.; Li, Y.C. A novel Tikhonov regularization- based iterative method for structural damage identification of offshore platforms. *J. Mar. Sci. Technol.* **2019**, *24*, 575–592. [CrossRef]
10. Bao, X.X.; Fan, T.X.; Shi, C.; Yang, G.L. One-dimensional convolutional neural network for damage detection of jacket-type offshore platforms. *Ocean Eng.* **2021**, *219*, 108293. [CrossRef]
11. Zargarzadeh, A.; Mojtahedi, A.; Mohammadyzadeh, S.; Hokmabady, H. Employing an improved cross model cross mode algorithm for damage detection of a steel offshore platform frame using experimental data. *Structures* **2020**, *28*, 1589–1600. [CrossRef]
12. Tang, D.; Chen, J.; Wu, W.H.; Xie, B.; Wang, S.S.; Feng, J.G. Research on sampling rate selection of sensors in offshore platform based on vibration. *Appl. Ocean Res.* **2020**, *101*, 102192. [CrossRef]
13. Barakat, N.; Mortadha, J.; Khan, A.; Abu-Nabah, B.A.; Al-Said, S.M. A one-dimensional approach towards edge crack detection and mapping using eddy current thermography. *Sens. Actuators A-Phys.* **2020**, *309*, 111999. [CrossRef]
14. Xu, Z.Y.; Jiang, Q.Q.; Zhang, Y.H.; Wu, J.B.; Li, L.; Qiu, F.S.; Wang, Z. Scanning Induction Thermography for Bearing Ring Under AC-DC Composite Magnetization. *J. Nondestruct. Eval.* **2022**, *42*, 3. [CrossRef]
15. Dirahoui, W.; Menana, H.; Hinaje, M. Nondestructive Testing of Multilayer HTS Tapes by Using Eddy Current Thermography. *IEEE Trans. Appl. Supercond.* **2022**, *32*, 6602607. [CrossRef]
16. Ding, S.; Tian, G.Y.; Zhu, J.Z.; Chen, X.T.; Wang, Y.Q.; Chen, Y.M. Characterisation and evaluation of paint-coated marine corrosion in carbon steel using eddy current pulsed thermography. *NDT E Int.* **2022**, *130*, 102678. [CrossRef]
17. Lee, S.; Chung, Y.; Kim, W. Defect Recognition and Morphology Operation in Binary Images Using Line-Scanning-Based Induction Thermography. *Appl. Sci.* **2022**, *12*, 6006. [CrossRef]
18. Liang, X.; Peng, J.P.; Zhang, X.; Guo, J.Q.; Zhang, Y. Analysis of the RCF crack detection phenomenon based on induction thermography. *Appl. Opt.* **2022**, *61*, 4809–4816. [CrossRef]
19. Tu, Y.X.; Mei, H.W.; Liu, L.S.; Shen, Z.K.; Guo, C.J.; Wang, L.M. Transient thermal pattern separation and detection of conductive defects in composite insulators using eddy current pulsed thermography. *NDT E Int.* **2022**, *129*, 102653. [CrossRef]

20. Liu, Y.; Tian, G.Y.; Gao, B.; Lu, X.L.; Li, H.R.; Chen, X.T.; Zhang, Y.H.; Xiong, L.H. Depth quantification of rolling contact fatigue crack using skewness of eddy current pulsed thermography in stationary and scanning modes. *NDT E Int.* **2022**, *128*, 102630. [CrossRef]
21. Hernandez, J.; Fouliard, Q.; Vo, K.; Raghavan, S. Detection of corrosion under insulation on aerospace structures via pulsed eddy current thermography. *Aerosp. Sci. Technol.* **2022**, *121*, 107317. [CrossRef]
22. Zou, X.X.; Wang, L.B.; Wang, J.Q.; Liu, J.; Ma, H.; Bao, Y. Nondestructive evaluation of carbon fiber reinforced polymer (CFRP)-steel interfacial debonding using eddy current thermography. *Compos. Struct.* **2022**, *284*, 115133. [CrossRef]
23. Chen, Y.T.; Xu, Z.Y.; Wu, J.B.; He, S.; Roskosz, M.; Xia, H.; Kang, Y.H. A Scanning Induction Thermography System for Thread Defects of Drill Pipes. *IEEE Trans. Instrum. Meas.* **2022**, *71*, 350250.
24. Ren, C.; Bai, L.B.; Shi, R.L.; Zhang, J.; Zhang, X.; Chen, C. Measurement of current distribution using infrared thermography. *Rev. Sci. Instrum.* **2023**, *94*, 034713. [CrossRef] [PubMed]
25. Xie, J.; Xu, C.H.; Chen, G.M.; Huang, W.P.; Song, G.B. Automated identification of front/rear surface cracks in ferromagnetic metals based on eddy current pulsed thermography. *Infrared Phys. Technol.* **2022**, *126*, 104345. [CrossRef]
26. Zhang, X.; Saniie, J.; Bakhtiari, S.; Heifetz, A. Compression of Pulsed Infrared Thermography Data With Unsupervised Learning for Nondestructive Evaluation of Additively Manufactured Metals. *IEEE Access* **2022**, *10*, 9094–9107. [CrossRef]
27. Yi, Q.J.; Malekmohammadi, H.; Tian, G.Y.; Laureti, S.; Ricci, M. Quantitative Evaluation of Crack Depths on Thin Aluminum Plate Using Eddy Current Pulse-Compression Thermography. *IEEE Trans. Ind. Ind. Inform.* **2020**, *16*, 3963–3973. [CrossRef]
28. Oswald-Tranta, B.; Feistkorn, S.; Roessler, G.; Scherrer, M. Comparison of different inspection techniques for fatigue cracks. In *Thermosense: Thermal Infrared Applications XLII, Proceedings of the Conference on Thermosense—Thermal Infrared Applications XLII, Online, 27 April–8 May 2020*; SPIE: Bellingham, WA, USA, 2020.
29. Souridi, P.; Chrysafi, A.P.; Athanasopoulos, N.; Siakavellas, N.J. Simple digital image processing applied to thermographic data for the detection of cracks via eddy current thermography. *Infrared Phys. Technol.* **2019**, *98*, 174–186. [CrossRef]
30. Carslaw, H.S.; Jaeger, J.C. *Conduction of Heat in Solids*; Osford University Press: New York, NY, USA, 1959; pp. 99–102.